analytical chemistry

Article

Cite This: *Anal. Chem.* 2019, 91, 12890−12899

pubs.acs.org/ac

# Microfluidic Mechanotyping of a Single Cell with Two Consecutive Constrictions of Different Sizes and an Electrical Detection System

Mamiko Sano,[†,‡] Noritada Kaji,[*,‡,§,∥] Amy C. Rowat,[⊥] Hirotoshi Yasaki,[†,‡] Long Shao,[#] Hidefumi Odaka,[#] Takao Yasui,[†,‡,∥] Tetsuya Higashiyama,[□,¶] and Yoshinobu Baba[†,‡,■,○]

[†]Department of Biomolecular Engineering, Graduate School of Engineering, Nagoya University, Furo-cho, Chikusa-ku, Nagoya 464-8603, Japan

[‡]Institute of Nano-Life-Systems, Institutes of Innovation for Future Society, Nagoya University, Furo-cho, Chikusa-ku, Nagoya 464-8603, Japan

[§]Department of Applied Chemistry, Graduate School of Engineering, Kyushu University, Moto-oka 744, Nishi-ku, Fukuoka 819-0395, Japan

[∥]Japan Science and Technology Agency, PRESTO, 4-1-8 Honcho, Kawaguchi, Saitama 332-0012, Japan

[⊥]Department of Integrative Biology & Physiology, University of California Los Angeles, 610 Charles E Young Dr. East, Los Angeles, California 90095, United States

[#]AGC Inc., Suehiro 1-1, Tsurumi-ku, Yokohama City, Kanagawa 230-0045, Japan

[□]Institute of Transformative Bio-Molecules (ITbM), Nagoya University, Furo-cho, Chikusa-ku, Nagoya 464-8602, Japan

[¶]Division of Biological Science, Graduate School of Science, Nagoya University, Furo-cho, Chikusa-ku, Nagoya 464-8602, Japan

[■]Health Research Institute, National Institute of Advanced Industrial Science and Technology (AIST), Hayashi-cho 2217-14, Takamatsu 761-0395, Japan

[○]College of Pharmacy, Kaohsiung Medical University, 100, Shih-Chuan First Road, Kaohsiung, 807, Taiwan, R.O.C.

*Supporting Information*

**ABSTRACT:** The mechanical properties of a cell, which include parameters such as elasticity, inner pressure, and tensile strength, are extremely important because changes in these properties are indicative of diseases ranging from diabetes to malignant transformation. Considering the heterogeneity within a population of cancer cells, a robust measurement system at the single cell level is required for research and in clinical purposes. In this study, a potential microfluidic device for high-throughput and practical mechanotyping were developed to investigate the deformability and sizes of cells through a single run. This mechanotyping device consisted of two different sizes of consecutive constrictions in a microchannel and measured the size of cells and related deformability during transit. Cell deformability was evaluated based on the transit and on the effects of cytoskeleton-affecting drugs, which were detected within 50 ms. The mechanotyping device was able to also measure a cell cycle without the use of fluorescent or protein tags.

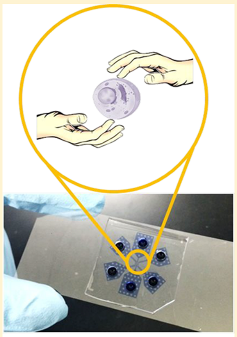

*Micropalpation on a chip*

The mechanical properties of cell mechanotypes are a potential and emerging biomarker for the noninvasive diagnosis of cells that reflects their intrinsic biochemical and biophysical properties. Cell mechanotyping has shown great potential in the early diagnosis and prognosis of cancer metastasis and may also have potential applications in regenerative medicine and cell transplantation. This is because it is noninvasive and offers an alternative label-free technique for selecting and collecting induced pluripotent stem cells (iPS) or adult human mesenchymal stem cells, which are currently needed. Various types of single cell mechanotyping techniques have been developed and include micropipette aspiration,[1] filtration,[2] optical tweezers,[3,4] atomic force microscopy (AFM),[5] microplate manipulation,[6,7] and magnetic tweezers.[8] Although these techniques focus on the use of precise and accurate forces to characterize cell mechanical properties, many of these methods are labor-intensive and have a low throughput. Therefore, the further development of robust cellular mechanotyping assay techniques is needed.

Recent developments in microfluidic devices have increased the throughput of mechanotyping measurements. Di Carlo et al. demonstrated the use of an automated microfluidic device to evaluate deformation of inertially focused cells in high-speed pinch flows and enabling a high throughput of 65000 cells/s.[9] They used their device to classify various cell types and to continuously enrich cells based on their size and deformability.[10−12] A rheology study on red blood cells was

**Received:** June 21, 2019
**Accepted:** August 23, 2019
**Published:** August 23, 2019

DOI: 10.1021/acs.analchem.9b02818
*Anal. Chem.* 2019, 91, 12890−12899

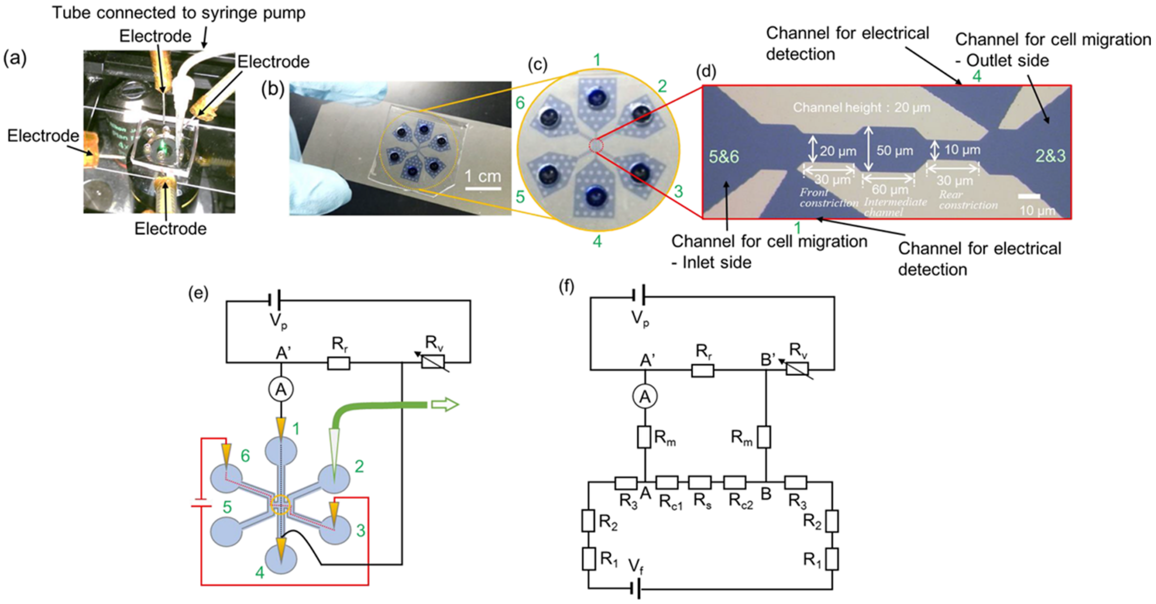

**Figure 1.** Overview of the experimental setup of the mechanotyping device based on an electrical detection system. (a) An image of the experimental setup consisting of the mechanotyping device, electrodes, and a tube for withdrawing solution. (b) An image of the mechanotyping device comprising PDMS microfluidic channels and a glass slide coverslip. (c) A magnified image of the mechanotyping device. The numbers in green show the reservoirs, and reservoir 2 was connected to a syringe pump. (d) An image of the consecutive constriction channel taken using a microscope. The dimensions of the channel and the positions of the reservoirs' are shown in the image. (e) A constant electric field (depicted in red) was applied across the detection area to maintain an electrical steady state for current measurement and to drive samples into the detection area. The fluctuation in current caused by the sample moving across the detection area was measured using the external electrical circuit (depicted in black). The syringe pump was connected to a reservoir through a silicone tube (depicted in green) and was operated in withdrawal mode to hydrodynamically drive cells into the detection area because the driving force by electrophoresis was insufficient to draw cells in the system. $R_r$ is a resistive element (~1 kΩ), and $R_v$ is a variable resistor. (f) General electrical circuit diagram of the current measurement system in the mechanotyping devices. $R_1$, $R_2$, and $R_3$ are the resistances of the microfluidic channels with different widths and lengths. $R_{c1}$, $R_{c2}$, and $R_s$ are the resistances of the front constriction channel, rear constriction channel, and spacing region, respectively.

performed using laser-induced cavitation bubbles.[13] The aforementioned techniques based on high-speed imaging provided high-throughput mechanotyping measurements, however, expensive high-speed cameras and high-end workstations are essential components. Passing cells through a narrow microchannel with a width or a height smaller than the cell dimension is an alternative and a simple approach to investigating cellular mechanical properties using a microfluidic chip. For instance, combining a 6 $\mu$m wide, 200 $\mu$m long, and 9.6 $\mu$m high microchannel with a dual photodiode detection system enabled the transit time required for a cell to pass through the constriction area to be measured. Differences in the transit times of HL60 cells, cytochalasin D-treated HL60 cells, and red blood cells were demonstrated semiquantitatively in a previous study.[14] A more detailed analysis of the transit time was achieved by investigating the elongation, speed, and entry phases of cells transiting through a narrow microchannel to probe the mechanical properties of brain cancer cells using a CCD camera[15] and a suspended microchannel resonator (SMR).[16] Jensen et al. incorporated two electrodes adjacent to a narrow microchannel (5 $\mu$m wide) and measured the resistance between these electrodes as a cell moved through the narrow microchannel.

The transit time differences of untreated and treated (with latrunculin) HeLa cells as they moved through the narrow microchannel provided semiquantitative results on cell deformability at a single cell level.[17] The effects of nuclear morphology of neutrophils on the mechanical properties of cells were investigated by measuring the total transit time of the cells through consecutive narrow spaces on a microfluidic chip. Using the cell deformability measurements, the expression level of lamin A was determined to have a significant effect on the mechanical properties of the cells.[18] Most of the aforementioned assay techniques rely on optical detection systems, such as high-speed CCD imaging, hence, their spatial resolution is limited to a few $\mu$m in the $xy$ plane.

Resistive-pulse sensing (RPS) is a potential alternative method, which is based on the detection of the ionic current blocking created when a particle transits a micropore or microchannel. RPS was developed in the 1950s and is known as the Coulter counter.[19] RPS is an extremely versatile technique which offers both higher spatial resolution (a few tens of nanometers in all directions) and higher time resolution (~MHz). However, a major drawback of the method is its narrow dynamic range which necessitates the adjustment of the pore or microchannel size to commensurate the size of the objectives. To address this issue, Sohn et al. attempted to develop node-pore sensing, through the addition of several nodes along the microchannel. This allowed for them to overcame the problems associated with the low signal-to-noise ratios of nanometer-sized objects coexisting with micrometer-sized objects and to isolate the distinct electronic signatures derived from large microscale cells and small nanoscale viruses.[20] This method was also applied in the profiling of surface-markers of single cells through the immobilization of antibodies on the microchannel surface. It demonstrated that RPS could be used to obtain a "fingerprint" of biochemical information for a single cell surface.[21,22] We attained high signal-to-noise ratios using a single channel size by isolating the detection circuit from the electrophoretic circuit,[23−26] as shown in Figure 1. Under the balanced potential state in the circuit in Figure 1, the background ionic currents in the detection circuit can be minimized. Transient currents are generated when a cell enters the constrictions channel, and the balanced potential is transiently collapsed (See Figure 1f). The potential difference between the ends of the resistive element (~1 kΩ), $R_r$, is set equal to that of the consecutive constriction channel by the variable resistance ($R_v$) before sample introduction. When the cell enters the consecutive constriction channel, the resistance value of the constrictions channel ($R_{c1} + R_s + R_{c2}$) increases, and the ionic current flow through the Amp meter increases. In our previous studies, in which we measured submicron sized particles, the voltage of the battery in the electrophoretic circuit, $V_f$, was enough to drive the sample.[23−26] However, for this cell measurement, the driving force by electrophoresis was insufficient to draw the cells into the constriction channel; therefore, a syringe pump was connected to a reservoir through a silicone tube, as shown in Figure 1a and 1e. The syringe pump operated in withdrawal mode, which allowed it to hydrodynamically drive the cells.

In this study, two different widths of constrictions were placed in a single detection microchannel to simultaneously enable cell sizing and deformability measurements using RPS as shown in Figure 1. The liner elasticity of cells within a small strain regime was determined through AFM indentation experiments, and the elastic modulus ranged between 0.1 and 100 kPa.[27−29] In large deformation, such as with our cell deformability measurements, Ding et al. reported that the surface tension had a remarkable effect on the indentation response beyond the elastic modulus.[30] The classification of cells as pure elastic bodies or as surface tension-dominant bodies does not dismiss, the potential effect that the sizes of the cells have on stress−strain relationship during the elongation process of the cells in the rear constriction. In our system, elongation elastic modulus in the rear constriction, $E$, was expressed as

$$E = \frac{\sigma}{\varepsilon}$$

In the above equation, $\sigma$ is stress (pressure by the hydrodynamic flow), and $\varepsilon$ is elongation strain given by

$$\varepsilon = (L - L_0)/L_0$$

In the above equation, $L_0$ and $L$ are the initial diameter and the elongated major-axis diameter in the rear constriction, respectively. Large cells deform and elongate much larger than small cells in the same cross-section area at the constriction. As a result, the residence time of larger cells at the rear constriction is expected to be longer than that of smaller cells. Considering the above factor, the cell size is an important factor in determining the residence time at the rear constriction. Therefore, the design of the consecutive constriction channel for sizing and deformability measurements of a single cell were adapted.

The proof of concept and validation of our system were conducted by taking simultaneous measurements on cells that had been treated with compounds, such as latrunculin A and paclitaxel to perturb their cytoskeletons. The detection system for determining cell size and deformability of cells was easy to operate; it provided precise information on cell deformability, including cell elasticity (as calibrated by the cell size), and allowed for moderate throughput (10−100 cells/s). The method also demonstrated cell cycle discrimination without any fluorescence labeling.

## MATERIALS AND METHODS

**Cell Culture.** HeLa cells (a cervical carcinoma cell line) and Jurkat cells (a human T-cell lymphoma cell line) were cultured at 37 °C in 5% $CO_2$ in the Minimum Essential Medium Eagle (MEM, M4655, Sigma-Aldrich Co. LLC., Tokyo, Japan) and the Roswell Park Memorial Institute 1640 Medium (RPMI1640, 11875093, Thermo Fisher Scientific Inc., Tokyo, Japan), respectively, supplemented with a 1% penicillin/streptomycin antibiotic mixture, 1% nonessential amino acids, and 10% fetal bovine serum (FBS) (which had been heat inactivated at 56 °C for 30 min before use).

**Drug Treatments for Cells.** The HeLa cells were treated with latrunculin A (Lat A; Wako Pure Chemical Industries, Ltd.) and paclitaxel (Pax; Wako Pure Chemical Industries, Ltd.) to induce changes in cell deformability. Lat A and Pax were added to a suspension of the HeLa cells with a density of $5 \times 10^5$ cells/mL to generate concentrations of 0.5 $\mu$M and 50 nM, respectively. The resultant solutions were incubated for 2 h at 37 °C in 5% $CO_2$.

**Cell Cycle-Dependent Collection by a Fluorescence-Activated Cell Sorter (FACS).** The HeLa cells were collected and resuspended in Dulbecco's Eagle Medium (DMEM) without phenol red (DMEM, High Glucose, HEPES, no Phenol Red, 21063-029, Thermo Fisher Scientific Inc., Tokyo, Japan) at a concentration of $2 \times 10^6$ cells/mL. To stain the nucleus, Hoechst33342 (Thermo Fisher Scientific Inc., Tokyo, Japan) was added to the cell suspension at a final concentration of 10 $\mu$g/mL. The suspension was incubated for 1 h at 37 °C in 5% $CO_2$. The cells were sorted by FACS and collected based on the intensity of their fluorescence based on the Hoechst 33342 using a cell sorter (Cell sorter SH800, Sony Corporation, Tokyo, Japan). The cells were also used for the deformability measurements.

**Ionic Current Detection System.** In our previous studies, we developed a system for the simultaneous detection of an ionic current and optical signal.[23−26] The device consists of two power supplies for electrophoresis and ionic current detection, that is, an ammeter and a 1-kΩ resistive element, respectively (e-Globaledge Corporation, Tokyo, Japan), and a variable-resistance element (Multi-Turn Precision Potentiometers, BI Technologies Japan Ltd., Tokyo, Japan). These components were connected to a lead and the electrical circuit is given in Figure 1c and 1d. According to the applied voltage for electrophoresis, the variable-resistance element in the detection circuit was adjusted to 0 A depending on the applied voltage for electrophoresis which results in no current flow into the detection circuit, before measurements. The resistance of the detection cell increases as the cell passes through the detection channel, and thus, the current bypasses the detection channel through the detection circuit. The current and the duration were proportional to the volume of cell and transit time in the detection channel, respectively, and were verified in the experiments. The driving force for the cell measurement by electrophoresis was insufficient to draw cells into the constriction channel; therefore, a syringe pump (KDS200, KD Scientific, Massachusetts, USA) was connected to a reservoir through a silicone tube, as shown in Figure 1a and 1b. It operated in withdrawal mode to hydrodynamically drive the cells. Prior to the measurements, the buffer conductivity was measured using a portable resistivity meter (LAQUA DS-70,

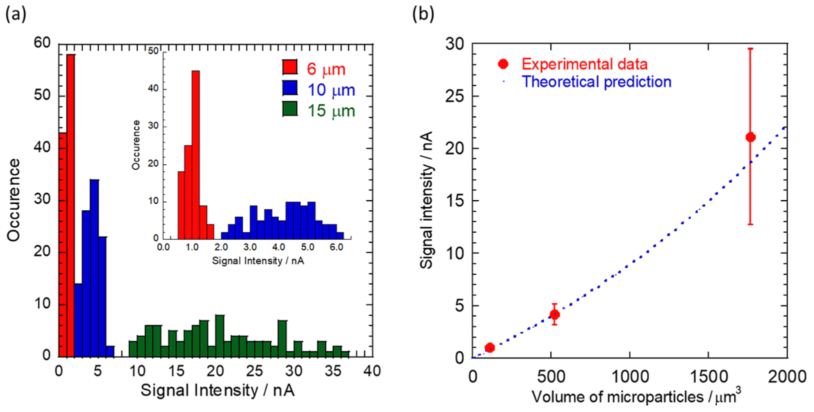

**Figure 2.** (a) Signal intensity histogram of polystyrene microparticles of 6, 10, and 15 $\mu$m in diameter were measured in a straight channel with a width of 20 $\mu$m and length of 20 $\mu$m ($N$ = 101, 101, and 99 for the 6, 10, and 15 $\mu$m microparticles, respectively). The inserted histogram is magnified in the region of low signal intensity. The measurement conditions were as follows: MEM medium with an electric conductivity of 1.414 S/m at 25 °C, 3 V for electrophoresis, and 5 $\mu$L/min for hydrodynamic flow. (b) Ensemble averaged signal intensities of the polystyrene microparticles (red dots). Errors bars indicate standard deviation. An equation for theoretical curve to estimate the sizes of the microparticles (blue dotted line) was, $\Delta i = (2.6979^{-10})R^3 + (1.4131^{-6})R^2 + 0.0072463R - 0.016252$, where $\Delta i$ is the detected current signal in nA and $R$ is the diameter of the target in $\mu$m.

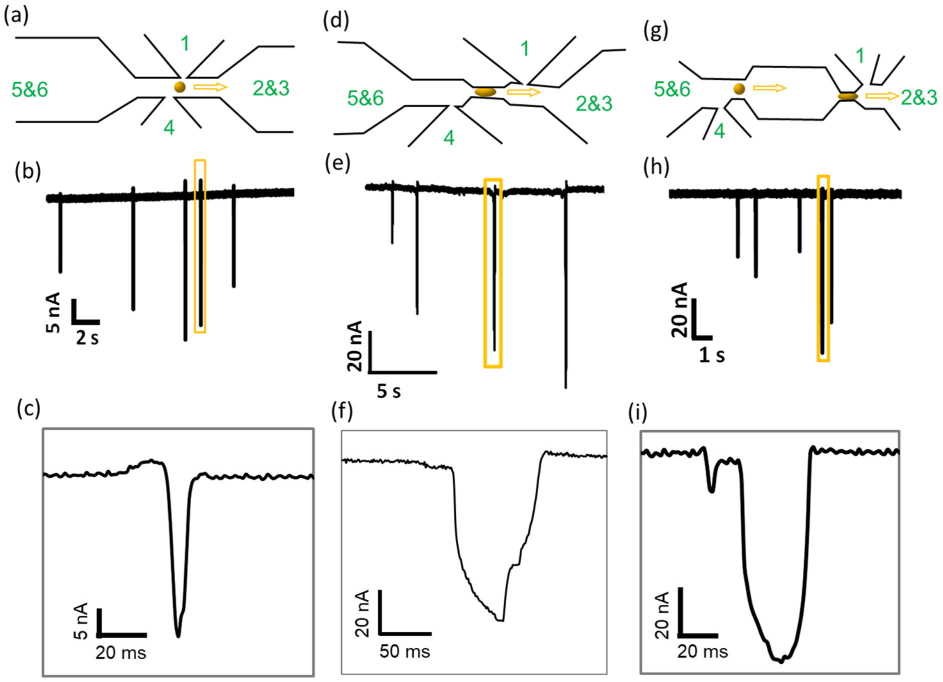

**Figure 3.** Relationship between the geometry of the microfluidic channels (a, d, and g) and the corresponding current signals derived from ion current blockades (b, e, and h) and their magnified signals (c, f, and i). The sample locations were observed by fluorescence microscopy, and each current signal was attributed to cell passage through the detection area as shown in Figure S1. (a−c) A straight channel with no constriction. Both the channel width and height are 20 $\mu$m and the length of the detection area is 20 $\mu$m. (d−f) A channel with a single constriction with a width of 10 $\mu$m and length of 40 $\mu$m. (g−i) A channel with one constriction with a width of 20 $\mu$m and length of 30 $\mu$m and a rear constriction with a width of 10 $\mu$m and length of 30 $\mu$m. The channel between the constrictions is 50 $\mu$m wide and 60 $\mu$m long. The microfluidic channels have the same height of 20 $\mu$m. (a, d, g) The numbers in green show the microchannel for electrical detection connected to the reservoirs depicted in Figure 1c.

Horiba, Ltd., Kyoto, Japan). A microchip was connected to the electrical circuit and was placed on an inverted microscope (Eclipse Ti, Nikon, Tokyo, Japan). The detection channel was observed during detection of the ionic current.

**CFD Simulation and Analysis.** A commercially available CFD package, and ANSYS Fluent (ANSYS, Inc., PA) were used for transient modeling of cells passing through the microchannel. The double-precision option was chosen to obtain enough accuracy because the dimensions were small, and the flow was multiphase. Numerical simulation was based on liquid drop model for a cell with given surface tension. The Euler−Euler (E-E) method was employed for transient tracking of the interface between the primary (medium) and the secondary (cell) phases. The E-E method for multiphase flows can support the liquid drop model and precisely predict the pressure drop due to surface tension by Laplace law. Patching is used to define the initial position of the cell in the simulation domain.

## RESULTS AND DISCUSSION

**Measurements of the Size of the Microparticles.** Precision and accuracy were validated by measuring polystyrene microparticles with 6, 10, and 15 $\mu$m diameters in a straight channel with a width of 20 $\mu$m, height of 20 $\mu$m, and length of 20 $\mu$m using the ionic current detection system. The results of the measurements are given in Figure 2a and 2b, which show the histograms and plots of the measurement results, respectively. Precision is relatively low for large microparticles because of the large CV (coefficient of variation) of the microparticle diameters used, that is, 15%, 15%, and 20% of microparticles with diameters of 6, 10, and 15 $\mu$m, respectively. However, considering propagation of uncertainty, the CVs with respect to the volumes of the particles were 26.0%, 26.0%, and 34.6% for the microparticles with diameters of 6, 10, and 15 $\mu$m microparticles, respectively. These CVs were comparable to the experimental values determined through the ionic current detection system, that is, 23.9%, 24.4%, and 35.6% for the microparticles with diameters of 6, 10, and 15 $\mu$m, respectively. The result confirmed a high precision of the measurements in the system. The experimental averages of the volumes of the microparticles were comparable to the theoretical prediction based on the signal intensities as shown in Figure 2b (see the Supporting Information). The comparison ensured the accuracy of the ionic current detection system as well as the precision.

**Size Measurements of the Cells.** The sizes of two different types of cells, that is, the HeLa and Jurkat cells, were measured and estimated using the microfluidic channel as shown in Figures 3a and S1a. The results of the detected signals are presented in Figure S2a and S2b, which show a histogram of the detected signal intensity and the estimated cell size based on the theoretical curve, respectively. The mean converted volumes of the HeLa and Jurkat cells were 1590 ± 419 (mean ± standard deviation) ($n$ = 50) and 808 ± 480 $\mu m^3$ ($n$ = 53), respectively, and the diameters were 14.3 ± 1.5 and 11.2 ± 2.0 $\mu$m, respectively. The Wilcoxon−Mann−Whitney test was conducted to determine statistical differences between the different groups of cells. These values are also in agreement with the results obtained by Deman et al. and Cartagena-Rivera et al.,[31,32] of 14.5 ± 1.6 and 11.5 ± 1.5 $\mu$m, respectively.

In our ionic current detection system, the obtained signal intensity was linearly proportional to the electrophoretic voltage over a wide range; therefore, a larger electrophoretic voltage resulted in a more intense signal and higher sensitivity. To optimize the electrophoretic voltage for the cell size measurements, the signal intensities were detected over a wide range of electrophoretic voltage (i.e., 3−53 V).There was a linear incremental relationship between the signal intensities and the electrophoretic voltage up to 40 V as shown in Figure S3. However, at 53 V, the cells ruptured in the detection channel possibly due to the strong electric field around the detection region (~170 V/cm), which is comparable to the electric field used in electroporation experiments. To minimize cell damage, the lowest electrophoretic voltage (3 V) was used in the following experiments.

**Residence Duration of the Cells in the Constrictions.** Selection of the constriction size is essential for cell deformability measurements. The mean diameter of the HeLa cells was determined to be 14.3 ± 1.5 $\mu$m; hence, a constriction channel with a width of 10 $\mu$m, a height of 20 $\mu$m, and a length of 30 $\mu$m was used as shown in Figures 3d and S1b. This allowed for the measurement of cell deformability. Untreated HeLa cells and Lat A-treated HeLa cells were analyzed using the ionic current detection system under the same conditions. In the cell size measurements, the signal intensities and the duration of residence in the constriction channel were measured. The results of the signal intensities obtained through the constriction channel were a magnitudes greater in comparison to the signal intensities in the straight channel with a width of 20 $\mu$m. This was probably because the temporal ion shielding which occurs when a cell is plugged into the constriction channel, resulting in the restricted flow of ions. In addition, the cells spent more time in the constriction than in the straight channel because the cells underwent deformation at the entrance and exit of the constriction, and transportation across the constriction was slower because of increased surface friction. The measured residence times were 22.6 ± 20.0 and 8.1 ± 7.7 ms for the untreated and Lat A-treated HeLa cells, respectively, as shown in Figure S4. The differences in the residence times are possibly due to changes in the deformability of HeLa cells as a result of their treatment with Lat A, which prevents actin polymerization and decreases cytoskeleton tension.[33,34]

**Consecutive Measurements of Cell Size and Deformability.** A microchannel containing two consecutive constrictions inside the ionic current detection area was fabricated, as shown in Figures 3g. The microchannel was designed to measure two parameters of a single cell, that is, cell size and deformability in a single run. The method was optimized and validated using an integrated microchannel, which comprised of a straight channel for cell size measurements and a constriction for cell deformability measurements. We assessed how the geometrical asymmetry and intermediate channel dimensions affect ionic current detection. As shown in Figure S5, the microchannel that the HeLa cells were introduced into contains two constrictions with the same width that are connected through a wide intermediate channel. Regardless of the width of the constrictions, which was adjusted for the cell size measurements (Figure S5c) and cell deformability measurements (Figure S5d), the symmetrical constrictions gave symmetrical signals and showed good correlation coefficients between the signal intensities of the front and rear signals (Figure S4e and S4f) of 0.94332 and 0.99031 for the cell size ($n$ = 44) and deformability measurements ($n$ = 100), respectively.

Separation of the ionic current signals of the front and rear is important for resolving the cell size and deformability information. Four different sizes of wide intermediate channels shown in Figure S6 were investigated in the process of optimizing the intermediate channel dimensions. The longer and wider intermediate channel promoted the resolution of the peaks corresponding to cell size and deformability. However, since a longer intermediate channel increases the probability of the successive introduction of cells, a 50 $\mu$m wide and a 60 $\mu$m long intermediate channel were chosen for the remainder of the experiments.

In the mechanotyping device we developed, each cell experienced both hydrodynamic and electrophoretic forces during transit through the microchannel. At the entrance of the rear constriction, the hydrodynamic pressure was theoretically calculated as 160 Pa ($1.6 \times 10-9$ N/$\mu m^2$), which translates to a force of $3.2 \times 10-8$ N for a cell at the entrance of a 10 × 20 $\mu m^2$ constriction channel area (for more details, see Supporting Information). The determined hydrodynamic

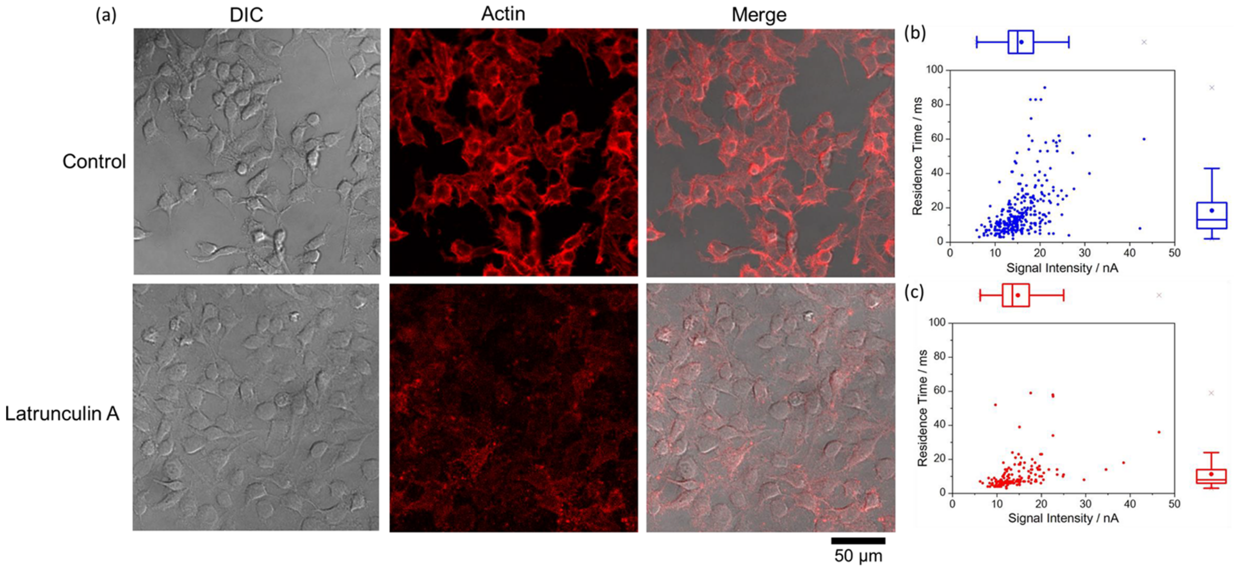

**Figure 4.** Evaluation of the size and deformability of HeLa cells treated with latrunculin A using a microchannel with two consecutive constrictions. The two constrictions had widths of 20 and 10 $\mu$m and were connected by a microchannel that was 50 $\mu$m wide and 60 $\mu$m long in the detection area. (a) Differential interference contrast (DIC) and fluorescence and merged images without latrunculin A (upper) and after treatment with Latrunculin A (lower). (b, c) The residence times of the HeLa cells without latrunculin A ($N$ = 317, blue dots) (b) and after treatment with latrunculin A ($N$ = 149, red dots) (c) at the rear constriction (10 $\mu$m wide) as a function of the current signal intensity, which corresponds to the cell size, detected at the front constriction (20 $\mu$m wide). The horizontal boxplots appeared in the top margins and the vertical boxplots appeared in the right margins represent the signal intensities and the residence time, respectively.

pressure was comparable to the reported values required to deform various kinds of cells, for example, 1.2−1.7 × 10−9 N/$\mu$m$^2$ in traction and 3−4 × 10−10 N/$\mu$m$^2$ in compression for fibroblasts 6, 1.5−3.0 × 10−10 N/$\mu$m$^2$ for fibroblast protrusions,[35] and 0.1−1 × 10−9 N/$\mu$m$^2$ for neurites.[36] The fluid velocity in the channel between the constrictions with no contact with the walls was determined as 40 $\mu$m/s, and the Stokes force acting on a 14 $\mu$m diameter spherical cell was 4.7 × 10−12 N. The abrupt increase of force by three to 4 orders of magnitude is possibly an important factor for the deformation of cells to enable their successful entry into the rear constriction without clogging. Concurrently, the electrophoretic force acting on a 14 $\mu$m diameter spherical cell was calculated based on Coulomb's law ($F = qE$), where $F$ is the force, $q$ is the charge of the cell, and $E$ is the electric field. The cell membrane capacitance and plasma membrane potential were assumed to be 2.0 $\mu$F/cm$^2$[37] and −50 mV,[38−40] respectively. The calculated electrophoretic force for the 14 $\mu$m diameter spherical cell was 2.4 × 10−9 N, and 1 order of magnitude smaller than the hydrodynamic force determined at the entrance of the rear constriction. It was also 3 orders of magnitude greater than the force in the intermediate channel. The results suggest that the dominant force in cell migration are dependent on their location; and the hydrodynamic pressure changes before and after a cell enters and plugs the rear constriction must be fully elucidated. This is because the volume of the fluid was only controlled through one reservoir in the system and the other reservoir acted as a pressure relief valve. After the cell enters the rear constriction, the deformed cell plugs the constriction and prevents hydrodynamic flow because of a loss of pressure balance. This leads to a pressure loss at the rear constriction of approximately 1/1000 (assuming a cell is a nonpermeable rigid sphere). However, in reality, a cell is flexible and can potentially deform into the corners of the channel; therefore, it has the potential to further prevent the flow. This may result in the electrophoretic force superseding the hydrodynamic force in facilitating movement of the cell within the rear constriction. The transit velocity ranged between 1 and 30 $\mu$m/ms and was faster than the hydrodynamic flow velocity of 0.2 $\mu$m/ms, which was determined for inside the rear constriction channel.

If a cell migrates with constant velocity, the Coulomb force acting on the cell balances with the Stokes viscous drag force can be determined using $qE = 6\pi\eta rv$, where $q$ is the charge of the cell, $E$ is the electric field, $\eta$ is viscosity of water, and $v$ is the electrophoretic migration velocity of the cell. A force ($qE$) of 2.4 × 10−9 N was determined for a spherical cell with a diameter of 14 $\mu$m diameter spherical cell. The force ($6\pi\eta rv$), which is derived from the observed transit velocity, ranged between approximately 0.094−4.5 × 10−9 N for a deformed cell along constrictions of between 10 and 20 $\mu$m wide with the velocity ranging between 1 and 30 $\mu$m/ms. The results are within the range of the observed phenomenon from both a electrophoretic and a hydrodynamic force perspective. The results of the calculations suggest that a cell upon entering the rear constriction it experiences both hydrodynamic and electrophoretic forces resulting in deformation; however, inside the rear constriction, the electrophoretic force is the dominant force, which results in cell movement.

During transit through the rear constriction, the cell is in direct contact with the right and left microchannel walls and occasionally the top or bottom walls. A nanometer-scale gap exists between the PDMS surface and glycosylated phospholipid cell membrane surface, and it has a lubricating film consisting of both free-flowing water molecules and hydrated water molecules on the siloxane and polysaccharides. The contacts across the lubricating film reflecting the physiological status of cells yield friction and uniformly suppress the transit velocity, however, the quantitative treatment of the friction force is complicated. The primary focus of our work was to

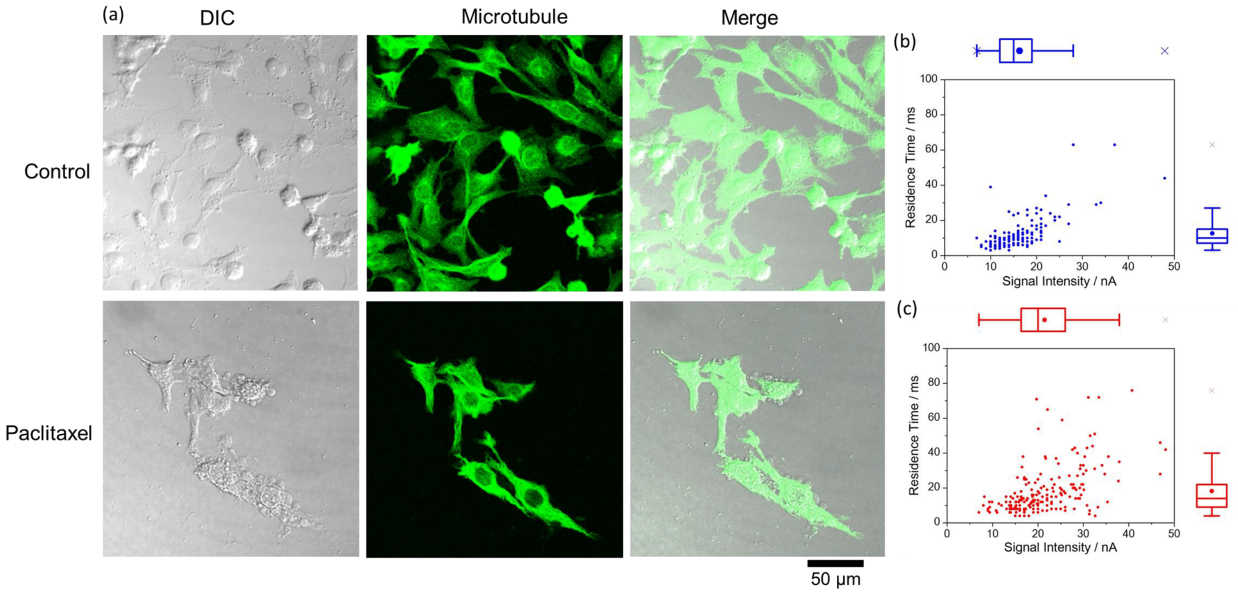

**Figure 5.** Evaluation of the size and deformability of HeLa cells treated with paclitaxel using a microchannel with two consecutive constrictions. The channel geometry was the same as that described in Figure 4. (a) Differential interference contrast (DIC), and fluorescence and merged images without paclitaxel (upper) and after treatment with paclitaxel (lower). (b, c) The residence time of the HeLa cells without paclitaxel ($N$ = 139, blue dots) (b) and after treatment with paclitaxel ($N$ = 201, red dots) (c) in the rear constriction (10 $\mu$m wide) as a function of the current signal intensity, which corresponds to the cell size, detected at the front constriction (20 $\mu$m wide). The horizontal boxplots appeared in the top margin and the vertical boxplots appeared in the right margin represent the signal intensities and the residence time, respectively.

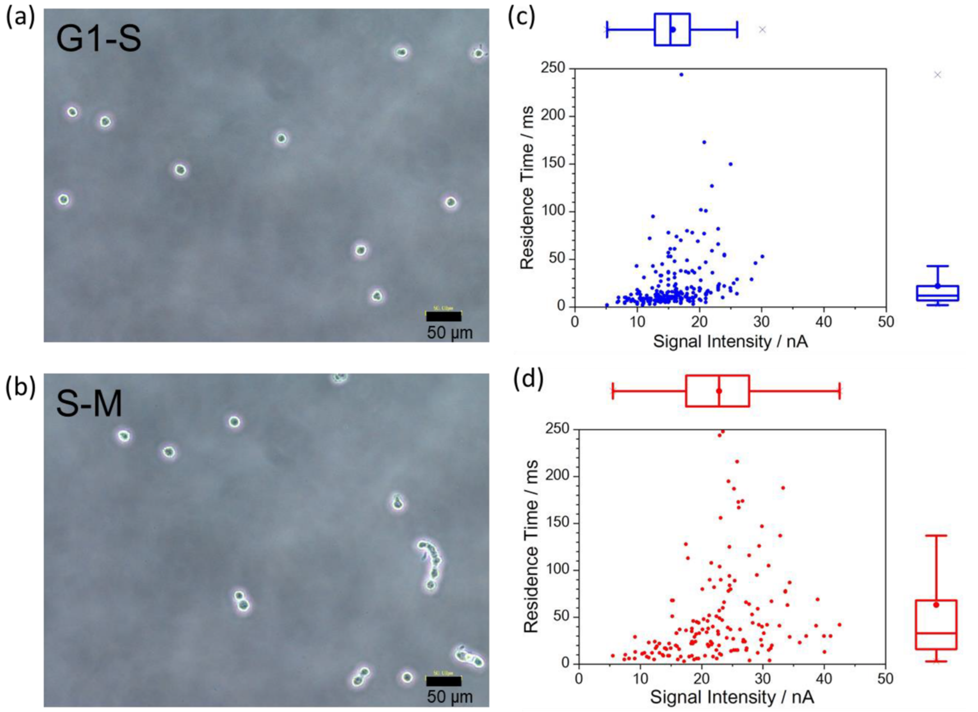

**Figure 6.** Evaluation of the size and deformability of HeLa cells depending on the cell cycle. The channel geometry was the same as that described in Figure 4. Phase contrast images of HeLa cells in G1/S (a) and S/M phase (b). (c, d) The residence time of the G1/S phase HeLa cells ($N$ = 167, blue dots) (c) and S/M phase HeLa cells ($N$ = 236, red dots) (d) in the rear constriction (10 $\mu$m wide) as a function of the current signal intensity, which corresponds to the cell size, detected at the front constriction (20 $\mu$m wide). The horizontal boxplots appeared in the top margin and the vertical boxplots appeared in the right margin represent the signal intensities and the residence time, respectively.

develop devices that enable comprehensive elucidation of the mechanical properties of a cell; the calculation and interpretation of friction is beyond the scope of this Article.

**Cell Deformability of Cells Treated with Cytoskeleton-Perturbing Drugs.** The applicability of the mechanotyping device with two consecutive constrictions was demonstrated. The size and deformability of Lat A-treated (0.5 $\mu$M for 2 h incubation) and Pax-treated (50 nM for 2 h incubation) HeLa cells were measured using the mechanotyping device with two consecutive constrictions. The optical microscope did not reveal any changes in the morphologies of the cells after 2 h of treatment with Lat A and Pax, respectively, as shown in Figures 4 and 5. The cells were run through the mechanotyping device, and the signal intensities of the ionic current at the front constriction and the residence time in the rear constriction were plotted, as shown in Figures 4b and 5b. The results showed that the Lat A-treated HeLa cells had shorter residence times in comparison to the control cells even when the cells were the same size. In contrast, the Pax-treated HeLa cells had slightly longer residence times than the control cells.

This difference of residence times of Lat A- and Pax-treated HeLa cells is possibly due to the different mechanisms and activities of the drugs. Lat A sequesters G-actin and prevents F-actin assembly; it also stoichiometrically binds monomeric actin and can be used to block actin polymerization in cells. At concentrations of between 1 and 10 $\mu$M, Lat A causes depolymerization of the tumor cell cytoskeleton within a period of 10 min.[41] In contrast, Pax reversibly binds to polymerized tubulin and stabilizes the microtubule assembly. It results in the inability of chromosomes in achieving a metaphase spindle configuration, and the progression of mitosis and prolonged activation of the mitotic checkpoint triggers apoptosis or reversion to the G-phase of the cell cycle without cell division.[42] This arrests the G2/M cell cycle, and the ratio of large cells is increased and the size distribution might be enlarged in paclitaxel-treated cells.[43] Preventing polymerization of actin filaments might influence the tension of the cytoskeleton than prevent depolymerization because the cytoskeletal framework remains after drug treatment. Therefore, Lat A had a greater impact on the cell deformability in comparison to Pax, and they have different polymerization and depolymerization targets. In this experiment, the HeLa cells were treated with 2 different drugs for 2 h, and their "pharmacokinetics" inside each cell was not considered. Data on how the drug treatment affects cell deformability over time, as well as statistical data analysis,[44,45] is required for a more detailed discussion on mechanotyping in the future.

**Cell Cycle Measurements Using the Mechanotyping Device.** The deformability of cells during different phases of the cell cycle was investigated. Prior to mechanotyping, the HeLa cells were separated and collected at different stages of the cell cycle using FACS. Cells that were in the G1 to S phases showed a narrower distribution of signal intensity and residence time in comparison to the cells that were in the S to M phases, as shown in Figure 6c and d. The results suggest that the cells in the G1 to S phases were smaller and had relatively uniform deformability. Some cells were in mitotic progression, and in this phase the longest diameter was almost double that of the cells in the G1 to S phases as shown in Figure 6b. At a low signal intensity, that is, approximately 20 nA, the residence time of both cell cycles were comparable; however, above 20 nA, the residence times of the cells in the S to M phases did not have a distinct distribution pattern. This was possibly due to the multiplication, that is, doubling of the quantity of genomes during the DNA replication process in the S phase and the progression of the chromosome condensation toward mitosis. Therefore, the cells were less deformable than those in the G1 to S phases.

Further studies are required to elucidate whether these signals are also reflective of the state inside a cell and whether it includes the cell nucleus or not. The method, does not require the labeling by fluorescence dyes or genetically coded proteins, and has the potential to serve as a new cell cycle determination tool.[46]

All the measurements in this Article were performed using suspended cells even in case of the adherent cells (HeLa cells). The treatment time and the concentration of trypsin used to detach HeLa cells from the culture flasks potentially had an effect on the residence time of the cells at the rear constriction because the changes in the interaction between the cells and the wall surfaces changed and were dependent on the degree of degradation of adhesive proteins, such as integrin in filopodia. The quantitative treatment of the friction force including the aforementioned chemical interaction is complicated and beyond the scope of this Article; it may pose a future challenge in microfluidic mechanotyping.

Computational fluid dynamics (CFD) simulation and analysis was conducted to validate the cell migration velocity and the hydrodynamic pressure in the microchannel as shown in Figure S7. The mode of the constant flow rate was also adopted in the cell deformability measurements. Therefore, the pressure applied to a migrating cell in the microchannel varied over time depending on the cell location, cell size, cell deformability, etc. Hydrodynamic pressure at the entrance of the rear constriction was calculated as 160 Pa without cell migration. When a cell enters the microchannel, the calculations may become more complicated when several parameters were considered. The CFD simulation results are presented in Figure S7. Figure S7c and S7d showed that the hydrodynamic pressure was at approximately 1.5 kPa when the cell entered into the rear constriction.

A fluid velocity plot at position 4, which represents the entrance of the rear constriction, shows the cell migration behavior in the constriction channel and is given in Figure 7f. The results show that the velocity dropped between 48 and 60 s to a minimum of 3 mm/s, after which it rapidly increased to a maximum of 6 mm/s. This result suggests that the migration behavior cells in the constriction channel is not constant.

## ■ CONCLUSION

In conclusion, a microfluidic-based mechanotyping device was developed to assay cell deformability. Latrunculin A and paclitaxel were applied to HeLa cells, and the deformability changes were observed using the device. The results were used to predict the forces necessary to deform the cells as well as the residence time in the rear constriction. Differences in residence times were attributed to the different action mechanism of the different drugs on the cells. The cell cycle was detected without any pretreatment of the cells with fluorescence dyes or protein tags. Therefore, the proposed system which integrates a cell-sorting system into a mechanotyping device has significant potential as a novel cell assay and recovery system for future regenerative medicine and cell transplantation.

## ■ ASSOCIATED CONTENT

### Ⓢ Supporting Information

The Supporting Information is available free of charge on the ACS Publications website at DOI: 10.1021/acs.analchem.9b02818.

> Theoretical calculations of the current signals, theoretical calculations of the hydrodynamic resistances, fluorescence microscope images of the migrating cells in the constriction channels, size measurements of Jurkat and HeLa cells, dependence of the current signal

intensity as a function of the driving voltage, residence time of HeLa cells with and without Lat A in the single constriction microchannel, evaluation of the relationship between the current signals and microchannel design, evaluation of the middle microchannel design, and CFD simulation and analysis results of the mechanotyping device (PDF)

CFD simulation (AVI)

## ■ AUTHOR INFORMATION

### Corresponding Author

*E-mail: kaji@cstf.kyushu-u.ac.jp.

### ORCID

Noritada Kaji: 0000-0002-9828-873X
Hirotoshi Yasaki: 0000-0001-6985-9073
Takao Yasui: 0000-0003-0333-3559

### Author Contributions

M.S., N.K., and A.R. designed the research; M.S., N.K., H.Y., L.S., H.O., and T.Y. conducted the experiments and analyzed the data; T.H. and Y.B. provided a fruitful basis for the data interpretation; and N.K., L.S., and A.R. wrote the paper.

### Notes

The authors declare no competing financial interest.

## ■ ACKNOWLEDGMENTS

This work was supported by Japan Science and Technology Agency (JST), PRESTO (No. JPMJPR16F4, No. JPMJPR151B), the Center of Innovation Program from JST, Nanotechnology Platform Program (Molecule and Material Synthesis) of the Ministry of Education, Culture, Sports, Science and Technology (MEXT) of Japan, a JSPS Grant-in-Aid for Scientific Research (A) 24241050, and the research grant from The Nitto Foundation. N.K. would like to express thanks to Ms. Yoko Suzuki and Ms. Hikaru Nakamura for their technical assistance.

## ■ REFERENCES

(1) Hochmuth, R. M. *J. Biomech* **2000**, *33*, 15−22.

(2) Gifford, S. C.; Frank, M. G.; Derganc, J.; Gabel, C.; Austin, R. H.; Yoshida, T.; Bitensky, M. W. *Biophys. J.* **2003**, *84*, 623−633.

(3) Lautenschlager, F.; Paschke, S.; Schinkinger, S.; Bruel, A.; Beil, M.; Guck, J. *Proc. Natl. Acad. Sci. U. S. A.* **2009**, *106*, 15696−15701.

(4) Ananthakrishnan, R.; Guck, J.; Wottawah, F.; Schinkinger, S.; Lincoln, B.; Romeyke, M.; Moon, T.; Kas, J. *J. Theor. Biol.* **2006**, *242*, 502−516.

(5) Rotsch, C.; Jacobson, K.; Radmacher, M. *Proc. Natl. Acad. Sci. U. S. A.* **1999**, *96*, 921−926.

(6) Thoumine, O.; Ott, A. *J. Cell Sci.* **1997**, *110* (Pt 17), 2109−2116.

(7) Guillou, L.; Babataheri, A.; Puech, P. H.; Barakat, A. I.; Husson, J. *Sci. Rep.* **2016**, *6*, 21529.

(8) Bausch, A. R.; Möller, W.; Sackmann, E. *Biophys. J.* **1999**, *76*, 573−579.

(9) Dudani, J. S.; Gossett, D. R.; Tse, H. T.; Di Carlo, D. *Lab Chip* **2013**, *13*, 3728−3734.

(10) Lin, J.; Kim, D.; Tse, H. T.; Tseng, P.; Peng, L. L.; Dhar, M.; Karumbayaram, S.; Di Carlo, D. *Microsystems & Nanoengineering* **2017**, *3*, 17013.

(11) Darling, E. M.; Di Carlo, D. *Annu. Rev. Biomed. Eng.* **2015**, *17*, 35−62.

(12) Hur, S. C.; Henderson-MacLennan, N. K.; McCabe, E. R.; Di Carlo, D. *Lab Chip* **2011**, *11*, 912−920.

(13) Quinto-Su, P. A.; Kuss, C.; Preiser, P. R.; Ohl, C.-D. *Lab Chip* **2011**, *11*, 672−678.

(14) Ji, Q. Q.; Du, G. S.; van Uden, M. J.; Fang, Q.; den Toonder, J. M. *Talanta* **2013**, *111*, 178−182.

(15) Khan, Z. S.; Vanapalli, S. A. *Biomicrofluidics* **2013**, *7*, 011806.

(16) Byun, S.; Son, S.; Amodei, D.; Cermak, N.; Shaw, J.; Kang, J. H.; Hecht, V. C.; Winslow, M. M.; Jacks, T.; Mallick, P.; Manalis, S. R. *Proc. Natl. Acad. Sci. U. S. A.* **2013**, *110*, 7580−7585.

(17) Adamo, A.; Sharei, A.; Adamo, L.; Lee, B.; Mao, S.; Jensen, K. F. *Anal. Chem.* **2012**, *84*, 6438−6443.

(18) Rowat, A. C.; Jaalouk, D. E.; Zwerger, M.; Ung, W. L.; Eydelnant, I. A.; Olins, D. E.; Olins, A. L.; Herrmann, H.; Weitz, D. A.; Lammerding, J. *J. Biol. Chem.* **2013**, *288*, 8610−8618.

(19) Coulter, W. H. *Proc. Natl. Electron Conf* **1956**, 1034−1040.

(20) Balakrishnan, K. R.; Anwar, G.; Chapman, M. R.; Nguyen, T.; Kesavaraju, A.; Sohn, L. L. *Lab Chip* **2013**, *13*, 1302−1307.

(21) Kim, J.; Han, S.; Lei, A.; Miyano, M.; Bloom, J.; Srivastava, V.; Stampfer, M. M.; Gartner, Z. J.; LaBarge, M. A.; Sohn, L. L. *Microsyst Nanoeng* **2018**, *4*, 17091.

(22) Balakrishnan, K. R.; Whang, J. C.; Hwang, R.; Hack, J. H.; Godley, L. A.; Sohn, L. L. *Anal. Chem.* **2015**, *87*, 2988−2995.

(23) Yasaki, H.; Yasui, T.; Yanagida, T.; Kaji, N.; Kanai, M.; Nagashima, K.; Kawai, T.; Baba, Y. *Sens. Actuators, B* **2018**, *260*, 746−752.

(24) Yasaki, H.; Yasui, T.; Yanagida, T.; Kaji, N.; Kanai, M.; Nagashima, K.; Kawai, T.; Baba, Y. *Chem. Lett.* **2018**, *47*, 350−353.

(25) Yasaki, H.; Shimada, T.; Yasui, T.; Yanagida, T.; Kaji, N.; Kanai, M.; Nagashima, K.; Kawai, T.; Baba, Y. *Acs Sensors* **2018**, *3*, 574−579.

(26) Yasaki, H.; Yasui, T.; Yanagida, T.; Kaji, N.; Kanai, M.; Nagashima, K.; Kawai, T.; Baba, Y. *J. Am. Chem. Soc.* **2017**, *139*, 14137−14142.

(27) Guo, Q. Q.; Xia, Y.; Sandig, M.; Yang, J. *J. Biomech.* **2012**, *45*, 304−309.

(28) Kuznetsova, T. G.; Starodubtseva, M. N.; Yegorenkov, N. I.; Chizhik, S. A.; Zhdanov, R. I. *Micron* **2007**, *38*, 824−833.

(29) Rosenbluth, M. J.; Lam, W. A.; Fletcher, D. A. *Biophys. J.* **2006**, *90*, 2994−3003.

(30) Ding, Y.; Xu, G. K.; Wang, G. F. *Sci. Rep.* **2017**, *7*, 45575.

(31) Cartagena-Rivera, A. X.; Logue, J. S.; Waterman, C. M.; Chadwick, R. S. *Biophys. J.* **2016**, *110*, 2528−2539.

(32) Deman, J. J.; Vakaet, L. C.; Bruyneel, E. A. *J. Membr. Biol.* **1976**, *26*, 189−204.

(33) Srivastava, V.; Robinson, D. N. *Curr. Biol.* **2015**, *25*, 663−670.

(34) Spector, I.; Shochet, N. R.; Blasberger, D.; Kashman, Y. *Cell Motil. Cytoskeleton* **1989**, *13*, 127−144.

(35) Felder, S.; Elson, E. L. *J. Cell Biol.* **1990**, *111*, 2513−2526.

(36) Dennerll, T. J.; Lamoureux, P.; Buxbaum, R. E.; Heidemann, S. R. *J. Cell Biol.* **1989**, *109*, 3073−3083.

(37) Asami, K.; Takahashi, Y.; Takashima, S. *Biophys. J.* **1990**, *58*, 143−148.

(38) Zhang, X.; Jin, Y.; Plummer, M. R.; Pooyan, S.; Gunaseelan, S.; Sinko, P. J. *Mol. Pharmaceutics* **2009**, *6*, 836−848.

(39) Szabo, I.; Brutsche, S.; Tombola, F.; Moschioni, M.; Satin, B.; Telford, J. L.; Rappuoli, R.; Montecucco, C.; Papini, E.; Zoratti, M. *EMBO J.* **1999**, *18*, 5517−5527.

(40) Stein, M. A.; Mathers, D. A.; Yan, H.; Baimbridge, K. G.; Finlay, B. B. *Infect. Immun.* **1996**, *64*, 4820−4825.

(41) Coue, M.; Brenner, S. L.; Spector, I.; Korn, E. D. *FEBS Lett.* **1987**, *213*, 316−318.

(42) Ganguly, A.; Yang, H.; Cabral, F. *Mol. Cancer Ther.* **2010**, *9*, 2914−2923.

(43) Trmcic, M. V.; Matovic, R. V.; Tovilovic, G. I.; Ristic, B. Z.; Trajkovic, V. S.; Ferjancic, Z. B.; Saicic, R. N. *Org. Biomol. Chem.* **2012**, *10*, 4933−4942.

(44) Leblanc-Hotte, A.; Sen Nkwe, N.; Chabot-Roy, G.; Affar, E. B.; Lesage, S.; Delisle, J.-S.; Peter, Y.-A. *Lab Chip* **2019**, *19*, 464−474.

(45) Sun, H.; Wang, S. *Data Mining and Knowledge Discovery* **2011**, *23*, 479−502.

(46) Otto, O.; Rosendahl, P.; Mietke, A.; Golfier, S.; Herold, C.; Klaue, D.; Girardo, S.; Pagliara, S.; Ekpenyong, A.; Jacobi, A.; Wobus,

M.; Topfner, N.; Keyser, U. F.; Mansfeld, J.; Fischer-Friedrich, E.; Guck, J. *Nat. Methods* **2015**, *12*, 199−202.